

Global changes in oceanic mesoscale currents over the satellite altimetry record

Josue Martinez-Moreno (✉ josue.martinezmorano@anu.edu.au)

The Australian National University <https://orcid.org/0000-0002-8348-1588>

Andrew Hogg

Australian National University <https://orcid.org/0000-0001-5898-7635>

Matthew England

UNSW Sydney <https://orcid.org/0000-0001-9696-2930>

Navid C. Constantinou

The Australian National University

Andrew E. Kiss

The Australian National University

Adele Morrison

Australian National University <https://orcid.org/0000-0002-9904-4980>

Article

Keywords: Oceanic eddies, oceanic mesoscale dynamics, climate change, mesoscale variability, satellite altimetry record

Posted Date: October 20th, 2020

DOI: <https://doi.org/10.21203/rs.3.rs-88932/v1>

License:  This work is licensed under a Creative Commons Attribution 4.0 International License.

[Read Full License](#)

Version of Record: A version of this preprint was published at Nature Climate Change on April 22nd, 2021. See the published version at <https://doi.org/10.1038/s41558-021-01006-9>.

Global changes in oceanic mesoscale currents over the satellite altimetry record

Josué Martínez-Moreno¹, Andrew McC. Hogg¹, Matthew H. England², Navid C. Constantinou¹, Andrew E. Kiss¹ & Adele K. Morrison¹

¹Research School of Earth Science and ARC Centre of Excellence for Climate Extremes, Australian National University, Canberra, ACT, Australia

²Climate Change Research Centre and ARC Centre of Excellence for Climate Extremes, University of New South Wales, Sydney, NSW, Australia

Oceanic eddies play a profound role in mixing tracers such as heat, carbon, and nutrients, thereby regulating regional and global climate. Yet, it remains unclear how global oceanic eddy kinetic energy has evolved over the past few decades. Furthermore, coupled climate model predictions generally fail to resolve oceanic mesoscale dynamics, which could limit their accuracy in simulating future climate change. Here we show a global statistically significant increase of the eddy activity using two independent observational datasets of mesoscale variability, one directly measuring currents and the other from sea surface temperature. Regions characterized by different dynamical processes show distinct evolution in the eddy field. For example, eddy-rich regions such as boundary current extensions and the Antarctic Circumpolar Current show a significant increase of 2% and 5% per decade in eddy activity, respectively. In contrast, most of the regions of observed decrease are found in the tropical oceans. Because eddies play a fundamental role in the ocean transport of heat, momentum,

21 **and carbon, our results have far-reaching implications for ocean circulation and climate, and**
22 **the modelling platforms we use to study future climate change.**

23 Changes in the climate system over recent decades have warmed the upper ocean and modi-
24 fied the wind stress, heat and freshwater fluxes that drive ocean circulation^{1,2}. These changes have
25 the capacity to modify the ocean circulation at all scales, including the overturning circulation^{3,4},
26 basin-scale gyres^{5,6}, boundary currents^{7,8}, and the mesoscale⁹. The ocean's mesoscale incorpo-
27 rates motions that occur at spatial scales from ~ 10 to ~ 100 km. These motions include both
28 steady flows, such as jets and re-circulations, and time-varying flows, generally referred to as ed-
29 dies. Mesoscale eddies are ubiquitous in the global ocean and feed back onto all scales, from
30 regional processes¹⁰ up to the meridional overturning circulation³. Moreover, these eddies act to
31 transport and mix tracers such as heat, salt, and nutrients^{11,12}. Thus, understanding the evolution
32 of the mesoscale circulation is crucial to better predict our changing oceans.

33 Kinetic energy (KE) quantifies the magnitude of ocean currents^{9,13-15}. Kinetic energy is
34 proportional to the square of the velocity, and is commonly separated into the mean KE (MKE;
35 computed from the time-mean velocity field) and the KE of the time-varying velocity (known as
36 the Eddy Kinetic Energy; EKE). The EKE is dominated by mesoscale variability and is a signifi-
37 cant fraction of the total KE^{16,17}. A recent study has inferred a global increase of KE anomaly from
38 ocean reanalyses and ARGO floats¹⁵. However, these reanalyses and observations do not have the
39 spatial resolution required to resolve the mesoscale field. Satellite observations, which can resolve
40 the mesoscale, suggest that EKE in the Southern Ocean has a robust increasing trend^{9,18,19}. How-

41 ever, there have been no studies that have quantified the global evolution of mesoscale variability
42 from satellite observations. This is the goal of the present study.

43 Mesoscale ocean flow has a footprint in both sea surface height (SSH) and sea surface tem-
44 perature (SST). EKE can be directly inferred from SSH via geostrophy, and mesoscale turbulence
45 also acts to strain and shear the temperature field, meaning that regions of high EKE are associated
46 with strong SST gradients. Therefore, observed gradients in SST can be considered a proxy for
47 mesoscale variability^{20–22}.

48 In this study, we examine the mesoscale evolution of the ocean from satellite observations of
49 sea surface height (SSH) and sea surface temperature (SST) over the available satellite altimetry
50 record (1993 - 2019). We use two independent datasets, namely AVISO+ SSH and NOAA optimal
51 interpolated sea surface temperature (OISST)²³, to estimate EKE and SST gradients respectively.
52 These fields are then temporally smoothed using a running average of 12 months; the trends and
53 the significance of each field are computed using a linear regression and a modified Mann–Kendall
54 test²⁴ (see Methods for further details). We explore the mesoscale time-series for the global ocean,
55 for individual ocean basins, and over regions characterized by their dynamical properties.

56 **Surface ocean acceleration**

57 Over recent decades, sea water thermal expansion and melting of land ice have led to an
58 increase of SSH^{1,25} (Fig. 1a). This SSH increase can be observed in all ocean basins, but there is
59 also regional variability (Fig. 1b). SSH gradients are proportional to the surface geostrophic flow,
60 from which we can compute velocity anomalies and Eddy Kinetic Energy (see Methods). The time-

61 mean EKE highlights mesoscale-rich regions including boundary currents and their extensions, the
62 Antarctic Circumpolar Current (ACC), and the equatorial band (Fig. 1d). More importantly, these
63 oceanic mesoscale-dominated sectors show significant trends over the satellite altimetry record
64 1993-2019 (Fig. 1f; and contours in Fig. 1d), which suggest a long-term adjustment of the global
65 ocean mesoscale field. In particular, the surface globally-integrated EKE trend is positive $\sim 0.56\%$
66 per decade (95% confidence level). The spatial structure of EKE trends is highly heterogeneous,
67 although its zonal average shows some significant net tendencies, with increasing trends polewards
68 of 25°S and 40°N (Fig. 1e,f). A strengthening of the EKE field is a direct indication of an increase
69 in mesoscale activity.

70 Sea Surface Temperature (SST) is an independent dataset relative to SSH, but is also influ-
71 enced by mesoscale activity and has better temporal and spatial resolution than SSH. SST has
72 increased on multi-decadal timescales due to climate change^{26,27} (Fig. 2a), with the global spatial
73 pattern also modulated by interdecadal climate variability. This increase is spatially heterogeneous,
74 with positive trends found in western boundary current regions⁷ and over much of the subtropical
75 gyres, and decreasing trends in the southeast Pacific, the far north Atlantic, and parts of the South-
76 ern Ocean (Fig. 2b). In contrast, the largest time-mean SST gradients are located in dynamic
77 mesoscale regions, such as boundary currents, their extensions, and the ACC (Fig. 2d). Regions
78 with large SST gradients also exhibit the largest positive SST gradient trends, while the subtropical
79 gyres and the tropics mostly exhibit a decreasing trend (Fig. 2e-f; contours in 2d). The globally
80 integrated SST gradient magnitude shows a significant increasing trend of 0.42% per decade (5.76
81 $\pm 2.46 \times 10^6 \text{ }^\circ\text{C m decade}^{-1}$; 95% confidence level) relative to the time-mean globally integrated

82 SST gradient magnitude ($1.36 \times 10^9 \text{ }^\circ\text{C m}$). Moreover, mesoscale eddies enhance the strength of
83 SST gradients on small length scales, and further analysis (Fig. S3) shows that mesoscale SST
84 gradients, characterized by features with horizontal length scales smaller than 3° , dominate the
85 observed trends. The globally integrated mesoscale SST gradient magnitude has increased at a
86 rate of $6.13 \pm 2.40 \times 10^6 \text{ }^\circ\text{C m decade}^{-1}$; significant at the 95% confidence level. The observed
87 SST gradient signal appears to be an intrinsic response to the mesoscale field, consistent with the
88 observed patterns of trends of the mesoscale EKE variability.

89 Eddy kinetic energy and mesoscale SST gradients show analogous spatial and temporal re-
90 sponses in the boundary currents and their extensions, the ACC and the tropics. Note that eddy-rich
91 regions such as the Kuroshio, the Agulhas, the Gulf Stream, and the ACC show large changes in
92 mesoscale SST gradients co-located with some of the largest EKE increases (Fig. 3). Even though
93 we do not expect the fields to match perfectly, the areas with same-sign trends match to a good
94 extent (Fig. S4). The similarity between these two independent satellite products reaffirms the
95 intrinsic response of the mesoscale processes to a changing and variable climate.

96 **Spatial patterns of ocean mesoscale trends**

97 Mesoscale EKE and SST gradient trends both indicate a net strengthening of the global
98 mesoscale. However, both datasets reveal heterogeneous patterns of trends. To further understand
99 the spatial variability, we first focus our analysis on individual area weighted regions: namely,
100 the Southern Ocean (south of 35°S), and the Pacific, Indian, and Atlantic Oceans north of 35°S
101 (Fig. 4d). This analysis reveals that the Southern Ocean and the Pacific Ocean are, to a large

102 extent, responsible for the globally integrated trends and variations of EKE and mesoscale SST
103 gradients; the trends in the Indian and Atlantic Oceans are in contrast much smaller (Fig. 4a,b).
104 The Southern Ocean shows a significant increase for both the EKE and SST gradient, however,
105 the Pacific Ocean SST gradient decreases significantly, while the EKE signal also decreases (albeit
106 below 95% significance level; Fig. 4c,e). The large uncertainty in the Pacific EKE trend (orange
107 error bars in Fig. 4c) is a consequence of the pulses in the time series during 1997 and 2015, both
108 being El Niño onset years. These large anomalous interannual signals dominate the uncertainty of
109 the global EKE trend, so that the global trends reported here are only just statistically significant
110 at the 95% confidence level.

111 Over the satellite altimetry record, the strongest El Niño events occurred during 1997-1998
112 and 2015-2016^{28,29} (gray bars in Fig. 4a,b). These El Niño events correlate with large pulses in the
113 Pacific EKE signal, resulting in large uncertainty in the calculated global trends (Fig. 4c). El Niño
114 events are associated with a strengthening of the North Equatorial Countercurrent and the northern
115 branch of the South Equatorial Current particularly during extreme eastern Pacific El Niños, such
116 as occurred during 1997-1998 and 2015-2016³⁰. During such El Niño events, the equatorial cur-
117 rents generate significant transient circulation anomalies extending over the equatorial band (9°N
118 - 9°S). After a scale decomposition of the velocities, we observe that these EKE pulses correspond
119 to features located within the equatorial band and have scales larger than the typical mesoscale
120 eddy size (see Methods; Fig. S5a,c). Thus, we conclude that modulation of the equatorial currents
121 during El Niño events are responsible for these distinct ~year-long EKE pulses.

122 To further investigate the effect of El Niño events on the mesoscale, we remove the equa-
123 torial regions (9°S – 9°N) and repeat the global trend analysis for EKE and SST gradients. The
124 globally integrated extratropical EKE and SST gradient trends increase, while the corresponding
125 uncertainty decreases; namely, EKE trends are now $1.46\% \pm 0.24\%$ per decade and SST gradi-
126 ents trends are $1.24\% \pm 0.17\%$ per decade (see striped bars in Fig. 4c,e); both significant at the
127 95% confidence level. It is thus clear that mesoscale activity in the Pacific, and particularly in the
128 equatorial region, is strongly influenced by interannual variability.

129 The observed changes in EKE and SST of whole ocean basins still integrate over large het-
130 erogeneous regions with opposing trends. For example, the Pacific Ocean aggregates the strength-
131 ening of the equatorial currents in the equatorial Pacific Ocean during El Niño events, boundary
132 currents, and the broader-scale oceanic gyres. These dynamical regions are not unique to the Pa-
133 cific Ocean; the Atlantic and Indian basins also span over diverse dynamical regions. Therefore,
134 we further decompose the ocean into dynamical regions (Fig. 5d): namely, the Antarctic Circum-
135 polar Current (ACC), the boundary currents and their extensions, the equatorial regions, and the
136 subtropical ocean gyres (see Methods for dynamical region definitions). The remaining regions
137 are grouped together. We now investigate the variability and trends within each of these dynamical
138 regions.

139 Globally, there is a significant increase of EKE and SST gradients, however, each dynami-
140 cal region shows a different response (Fig. 5). For example, the ACC region shows a significant
141 increase in both EKE and SST gradients, consistent with an increase in wind stress there, as demon-

142 strated in previous studies^{13,31}. Boundary currents and their extensions collectively show a similar
143 net response, in which EKE and SST gradients both increase. Individually, SST gradients increase
144 in all boundary currents, however EKE in the Agulhas retroflection, the East Australian Current,
145 the Leeuwin Current and the Malvinas Current have significantly increased, but the Gulf Stream
146 and the Kuroshio Current do not show a significant net strengthening^{32,33} (Fig. S6); instead, re-
147 gions of increase and decrease tend to cancel each other out in an area-average, particularly for
148 the Kuroshio Current (Fig. 1f). The response seen in the Gulf Stream and Kuroshio Currents is
149 consistent with the idea that these currents have shifted polewards^{7,34} and readjusted to climate
150 modes³⁵. Note that a poleward shift cannot be captured by our static climatological definition of
151 the boundary currents (see Methods). Moreover, regions outside the dynamical regions exhibit a
152 significant increase of EKE and SST gradients, comparable to those of the more energetic regions.
153 Thus, the observed increase of these remaining regions could be a consequence of the poleward
154 shift of the boundary currents, particularly in the Northern Hemisphere.

155 There are two dynamical regions that do not exhibit an increasing trend (Fig. 5). The equato-
156 rial region is, again, dominated by interannual variability, where the largest changes correspond to
157 El Niño events in both the EKE and mesoscale SST gradient time series. The mesoscale SST gradi-
158 ents show a significant decrease, which suggests a reduction of the mesoscale variability. However,
159 the equatorial EKE trends are insignificant, due to the dominance of interannual variability in the
160 signal. Similarly, subtropical gyre mesoscale SST gradients have decreased significantly over the
161 past few decades, while the EKE trend is negative, but not significant. This observed decrease
162 of SST gradients across the tropics and subtropics (Fig. 2) could result from the displacement of

163 the extratropical atmospheric circulation^{36,37} (Hadley cells) and expansion of the tropics³⁸, which
164 could explain the decreasing SST gradient trends in the tropics due to homogenization of the trop-
165 ical surface SST gradients. Thus, the SST gradients induced by mesoscale stirring are expected to
166 reduce as the surface ocean becomes more thermally homogeneous. However, a longer record is
167 required to separate the mesoscale response from interannual-decadal climate variability.

168 We have analysed the available satellite altimetry record of SSH and SST to reveal a signifi-
169 cant global intensification of the mesoscale field over the satellite record, where eddy-rich regions
170 such as boundary current extensions and the Antarctic Circumpolar Current present a significant
171 strengthening of 2% and 5% respectively. This increase is most apparent in regions where eddies
172 are already strong, such as the Southern Ocean as well as boundary currents and their exten-
173 sions. This mesoscale signature is observed in both eddy kinetic energy and mesoscale sea surface
174 temperature gradients. Note that these observed trends only capture the ocean's surface. If we
175 assume that the mesoscale flow extends vertically to around 500 m depth (a reasonable assump-
176 tion given the vertical structure of the gravest mode³⁹), then the EKE trends imply a significant
177 change in the global mesoscale energy budget of 0.42% - 0.93% ($0.05 - 0.12 \times 10^{18}$ Joules) over
178 the satellite altimetry record⁴⁰. Given the importance of mesoscale eddies for the redistribution of
179 carbon and heat by the oceans, in addition to their capacity to control climate on regional to global
180 scales, understanding this signal is crucial for improving future predictions of our oceans under
181 anthropogenic forcing. Furthermore, current generation climate models used for climate projec-
182 tions (CMIP6) do not generally resolve eddies⁴¹; thus, important climatic adjustments driven by
183 eddy-forced changes are likely to be missing from these simulations.

184 The mesoscale evolution described here cannot be captured by coarse-resolution reanalysis
185 products and sparse ARGO float observations, as previously used in other studies¹⁵. Here we used
186 eddy-permitting satellite observations to reveal an insignificant decrease in EKE over the tropics,
187 while reanalysis products suggest the tropics is where KE has recently increased the most. To
188 better understand this discrepancy, we revisited the analysis for the oceanic KE time-anomaly, as
189 undertaken by Hu et al.¹⁵, using our eddy-permitting satellite-derived KE. The results obtained are
190 almost identical to the trends we presented in the analysis above (Fig. S7), yet strikingly different
191 from those obtained by Hu et al. using non-eddy-resolving data (cf. their Fig 2a). This suggests that
192 the inability of reanalyses and the Argo dataset to resolve the mesoscale, due to coarse-resolution
193 and sparse sampling, leads to different estimates for regional kinetic energy trends. In addition, as
194 we have demonstrated, the tropics are strongly influenced by interannual variability (e.g. El Niño),
195 and yet the KE time-series from coarse reanalysis data do not detect the two extreme El Niño
196 events observed in the satellite record. Thus, data resolution is the likely cause of the discrepancy
197 between our eddy-permitting analysis and the results from the prior work using coarse-resolution
198 reanalysis products¹⁵.

199 We investigated several hypotheses in order to explain the observed trends including (1)
200 changes in winds (wind curl, wind stress), (2) changes in stratification, and (3) changes in large-
201 scale temperature gradients. The drivers of the observed trends are likely to be a combination of
202 (1) non-local increases of winds, (2) outcropping and tilting of isopycnals, and (3) strengthening
203 of baroclinic instability. However, the changes of winds, isopycnals and baroclinic growth rate are
204 small, highly variable and sparse. Thus, better observational records are required to understand

205 the increase in EKE observed from satellites. Moreover, as discussed above, coarse-resolution re-
206 analysis products differ significantly from the mesoscale evolution we could detect from observed
207 satellite altimetry. Thus, an in-depth analysis of the mesoscale evolution should be explored in
208 more detail using eddy-resolving global ocean models and/or reanalyses.

209 Our study has documented major global scale reorganisation of the ocean's mesoscale kinetic
210 energy observed over the past three decades. These observed adjustments in the mesoscale field
211 have the potential to affect ocean circulation at all scales, and to modify the transport and redistri-
212 bution of tracers, such as heat, carbon, and nutrients. Our findings thus have major implications
213 for ocean readjustment to a changing climate.

- 214 1. Pörtner, H. *et al.* IPCC, 2019: IPCC special report on the ocean and cryosphere in a changing
215 climate. *IPCC 2019* 42 (2019).
- 216 2. Intergovernmental Panel on Climate Change. Working Group 1, S. *et al.* *Climate Change 2007*
217 *- The Physical Science Basis: Working Group I Contribution to the Fourth Assessment Report*
218 *of the IPCC*. Assessment report (Intergovernmental Panel on Climate Change): Working
219 Group (Cambridge University Press, 2007).
- 220 3. Marshall, J., Scott, J. R., Romanou, A., Kelley, M. & Leboissetier, A. The dependence of the
221 ocean's MOC on mesoscale eddy diffusivities: A model study. *Ocean Modelling* **111**, 1–8
222 (2017).

- 223 4. Toggweiler, J. R. & Russell, J. Ocean circulation in a warming climate. *Nature* **451**, 286–8
224 (2008).
- 225 5. Yang, H. *et al.* Poleward Shift of the Major Ocean Gyres Detected in a Warming Climate.
226 *Geophysical Research Letters* **47** (2020).
- 227 6. Sutton, R. T. & Hodson, D. L. R. Climate Response to Basin-Scale Warming and Cooling of
228 the North Atlantic Ocean. *Journal of Climate* **20**, 891–907 (2007).
- 229 7. Wu, L. *et al.* Enhanced warming over the global subtropical western boundary currents. *Nature*
230 *Climate Change* **2**, 161–166 (2012).
- 231 8. Kwon, Y.-O. *et al.* Role of the Gulf Stream and Kuroshio–Oyashio Systems in Large-Scale
232 Atmosphere–Ocean Interaction: A Review. *Journal of Climate* **23**, 3249–3281 (2010).
- 233 9. Hogg, A. M. *et al.* Recent trends in the Southern Ocean eddy field. *Journal of Geophysical*
234 *Research: Oceans* **120**, 257–267 (2015).
- 235 10. Radko, T. & Marshall, J. Eddy-Induced Diapycnal Fluxes and Their Role in the Maintenance
236 of the Thermocline. *Journal of Physical Oceanography* **34**, 372–383 (2004).
- 237 11. Chelton, D. B., Gaube, P., Schlax, M. G., Early, J. J. & Samelson, R. M. The influence of
238 nonlinear mesoscale eddies on near-surface oceanic chlorophyll. *Science* **334**, 328–32 (2011).
- 239 12. Early, J. J., Samelson, R. M. & Chelton, D. B. The Evolution and Propagation of Quasi-
240 geostrophic Ocean Eddies. *Journal of Physical Oceanography* **41**, 1535–1555 (2011).

- 241 13. Meredith, M. P., Garabato, A. C., Hogg, A. M. & Farneti, R. Sensitivity of the Overturning
242 Circulation in the Southern Ocean to Decadal Changes in Wind Forcing. *Journal of Climate*
243 **25**, 99–110 (2012).
- 244 14. Busecke, J. J. M. & Abernathy, R. P. Ocean mesoscale mixing linked to climate variability.
245 *Science Advances* **5**, eaav5014 (2019).
- 246 15. Hu, S. *et al.* Deep-reaching acceleration of global mean ocean circulation over the past two
247 decades. *Science Advances* **6**, eaax7727 (2020).
- 248 16. Wyrтки, K., Magaard, L. & Hager, J. Eddy energy in the oceans. *Journal of Geophysical*
249 *Research* **81**, 2641–2646 (1976).
- 250 17. Chelton, D. B., Schlax, M. G., Samelson, R. M. & de Szoeke, R. A. Global observations of
251 large oceanic eddies. *Geophysical Research Letters* **34**, L15606 (2007).
- 252 18. Patara, L., Böning, C. W. & Biastoch, A. Variability and trends in Southern Ocean eddy activ-
253 ity in 1/12° ocean model simulations. *Geophysical Research Letters* **43**, 4517–4523 (2016).
- 254 19. Martínez-Moreno, J., Hogg, A. M., Kiss, A. E., Constantinou, N. C. & Morrison, A. K. Kinetic
255 energy of eddy-like features from sea surface altimetry. *Journal of Advances in Modeling*
256 *Earth Systems* **11**, 3090–3105 (2019).
- 257 20. Yuan, Y. & Castelao, R. M. Eddy-induced sea surface temperature gradients in Eastern Bound-
258 ary Current Systems. *Journal of Geophysical Research: Oceans* **122**, 4791–4801 (2017).

- 259 21. Castellani, M. Identification of eddies from sea surface temperature maps with neural net-
260 works. *International Journal of Remote Sensing* **27**, 1601–1618 (2006).
- 261 22. Holladay, C. G. & O’Brien, J. J. Mesoscale Variability of Sea Surface Temperatures. *Journal*
262 *of Physical Oceanography* **5**, 761–772 (1975).
- 263 23. Banzon, V., Smith, T. M., Steele, M., Huang, B. & Zhang, H.-M. Improved Estimation of
264 Proxy Sea Surface Temperature in the Arctic. *Journal of Atmospheric and Oceanic Technology*
265 **37**, 341–349 (2020).
- 266 24. Yue, S. & Wang, C. The Mann-Kendall Test Modified by Effective Sample Size to Detect
267 Trend in Serially Correlated Hydrological Series. *Water Resources Management* **18**, 201–218
268 (2004).
- 269 25. Polito, P. S. & Sato, O. T. Global Interannual Trends and Amplitude Modulations of the
270 Sea Surface Height Anomaly from the TOPEX/ Jason-1 Altimeters. *Journal of Climate* **21**,
271 2824–2834 (2008).
- 272 26. Cane, M. A. *et al.* Twentieth-Century Sea Surface Temperature Trends. *Science* **275**, 957–960
273 (1997).
- 274 27. Ruela, R., Sousa, M. C., deCastro, M. & Dias, J. M. Global and regional evolution of sea
275 surface temperature under climate change. *Global and Planetary Change* **190**, 103190 (2020).
- 276 28. Johnson, G. C., McPhaden, M. J., Rowe, G. D. & McTaggart, K. E. Upper equatorial Pacific
277 Ocean current and salinity variability during the 1996-1998 El Niño-La Niña cycle. *Journal*
278 *of Geophysical Research: Oceans* **105** (2000).

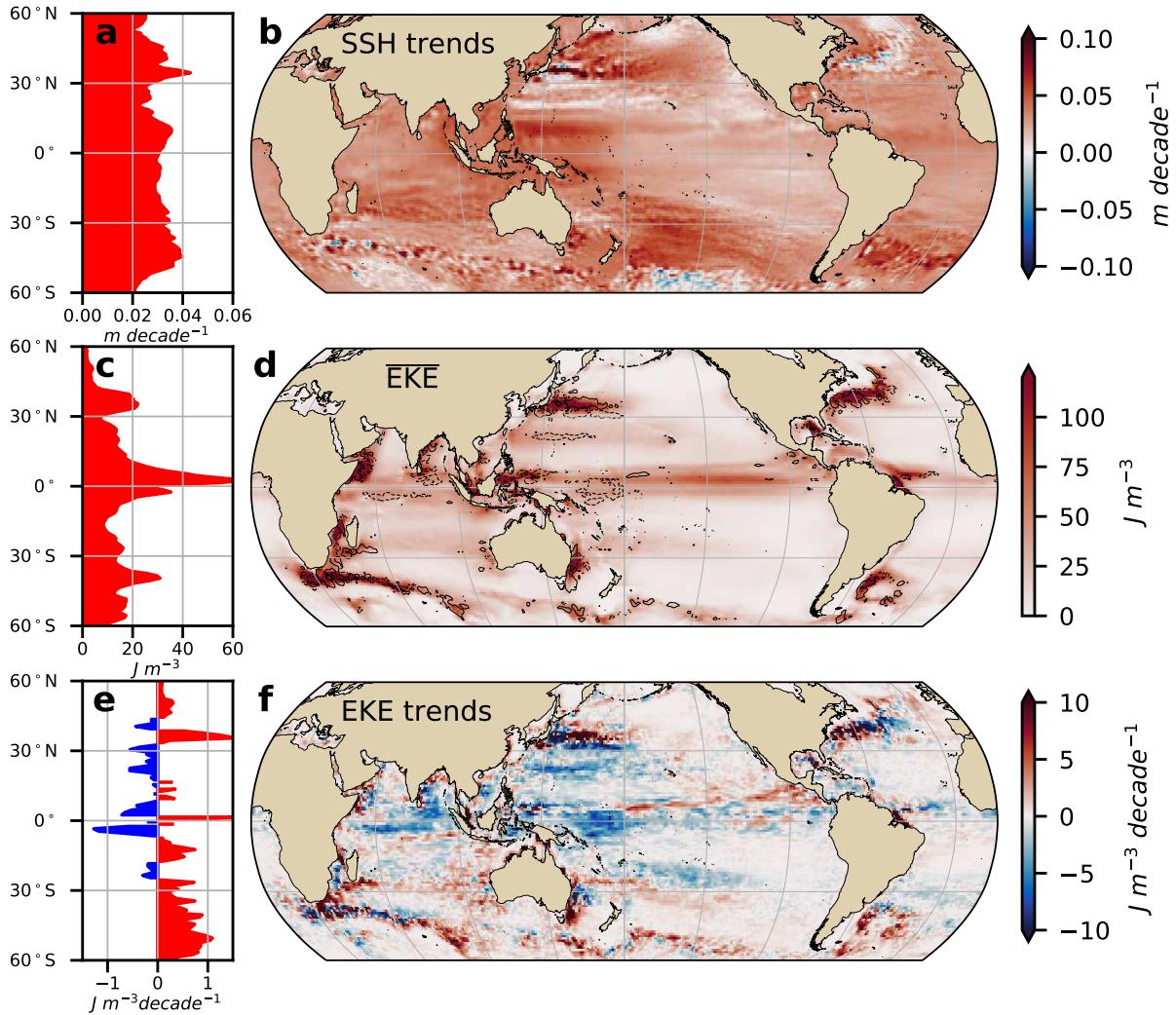
- 279 29. McPhaden, M. J. The child prodigy of 1997-98. *Nature* **398**, 559–561 (1999).
- 280 30. Wang, L.-C. & Wu, C.-R. Contrasting the Flow Patterns in the Equatorial Pacific Between
281 Two Types of El Niño. *Atmosphere-Ocean* **51**, 60–74 (2013).
- 282 31. Hughes, C. W. & Wilson, C. Wind work on the geostrophic ocean circulation: An observa-
283 tional study of the effect of small scales in the wind stress. *Journal of Geophysical Research:*
284 *Oceans (1978–2012)* **113**, C02016 (2008).
- 285 32. Ezer, T., Atkinson, L. P., Corlett, W. B. & Blanco, J. L. Gulf Stream’s induced sea level rise
286 and variability along the U.S. mid-Atlantic coast: Gulf Stream induces coastal sea level rise.
287 *Journal of Geophysical Research: Oceans* **118**, 685–697 (2013).
- 288 33. Uchida, H. & Imawaki, S. Estimation of the sea level trend south of Japan by combining
289 satellite altimeter data with in situ hydrographic data. *Journal of Geophysical Research* **113**
290 (2008).
- 291 34. Yang, H. *et al.* Intensification and poleward shift of subtropical western boundary currents in
292 a warming climate. *Journal of Geophysical Research: Oceans* **121**, 4928–4945 (2016).
- 293 35. Piecuch, C. G. Likely weakening of the Florida Current during the past century revealed by
294 sea-level observations. *Nature Communications* **11**, 3973 (2020).
- 295 36. Saenko, O. A., Fyfe, J. C. & England, M. H. On the response of the oceanic wind-driven
296 circulation to atmospheric CO₂ increase. *Climate Dynamics* **25**, 415–426 (2005).

- 297 37. Gupta, A. S. *et al.* Projected Changes to the Southern Hemisphere Ocean and Sea Ice in the
298 IPCC AR4 Climate Models. *Journal of Climate* **22**, 3047–3078 (2009).
- 299 38. Seidel, D. J., Fu, Q., Randel, W. J. & Reichler, T. J. Widening of the tropical belt in a changing
300 climate. *Nature Geoscience* **1**, 21–24 (2007).
- 301 39. Sanchez de La Lama, M., LaCasce, J. H. & Fuhr, H. K. The vertical structure of ocean eddies.
302 *Dynamics and Statistics of the Climate System* **1**, dzw001 (2016).
- 303 40. Wunsch, C. & Ferrari, R. Vertical mixing, energy and the general circulation of oceans. *Annual*
304 *Review of Fluid Mechanics* **36**, 281–314 (2004).
- 305 41. Haarsma, R. J. *et al.* High Resolution Model Intercomparison Project (HighResMIP v1.0) for
306 CMIP6. *Geoscientific Model Development* **9**, 4185–4208 (2016).
- 307 42. Wolter, K. & Timlin, M. S. Measuring the strength of ENSO events: How does 1997/98 rank?
308 *Weather* **53**, 315–324 (1998).
- 309 43. Lagerloef, G. S. E., Mitchum, G. T., Lukas, R. B. & Niiler, P. P. Tropical Pacific near-surface
310 currents estimated from altimeter, wind, and drifter data. *Journal of Geophysical Research:*
311 *Oceans* **104**, 23313–23326 (1999).

312 **Acknowledgments**

313 We thank Ryan Holmes for clarifying the equatorial response of El Niño events during
314 1997-1998 and 2015-2016. The satellite altimetry products were produced by Ssalto/Duacs and
315 distributed by AVISO+, with support from CNES (<https://www.aviso.altimetry.fr/>)

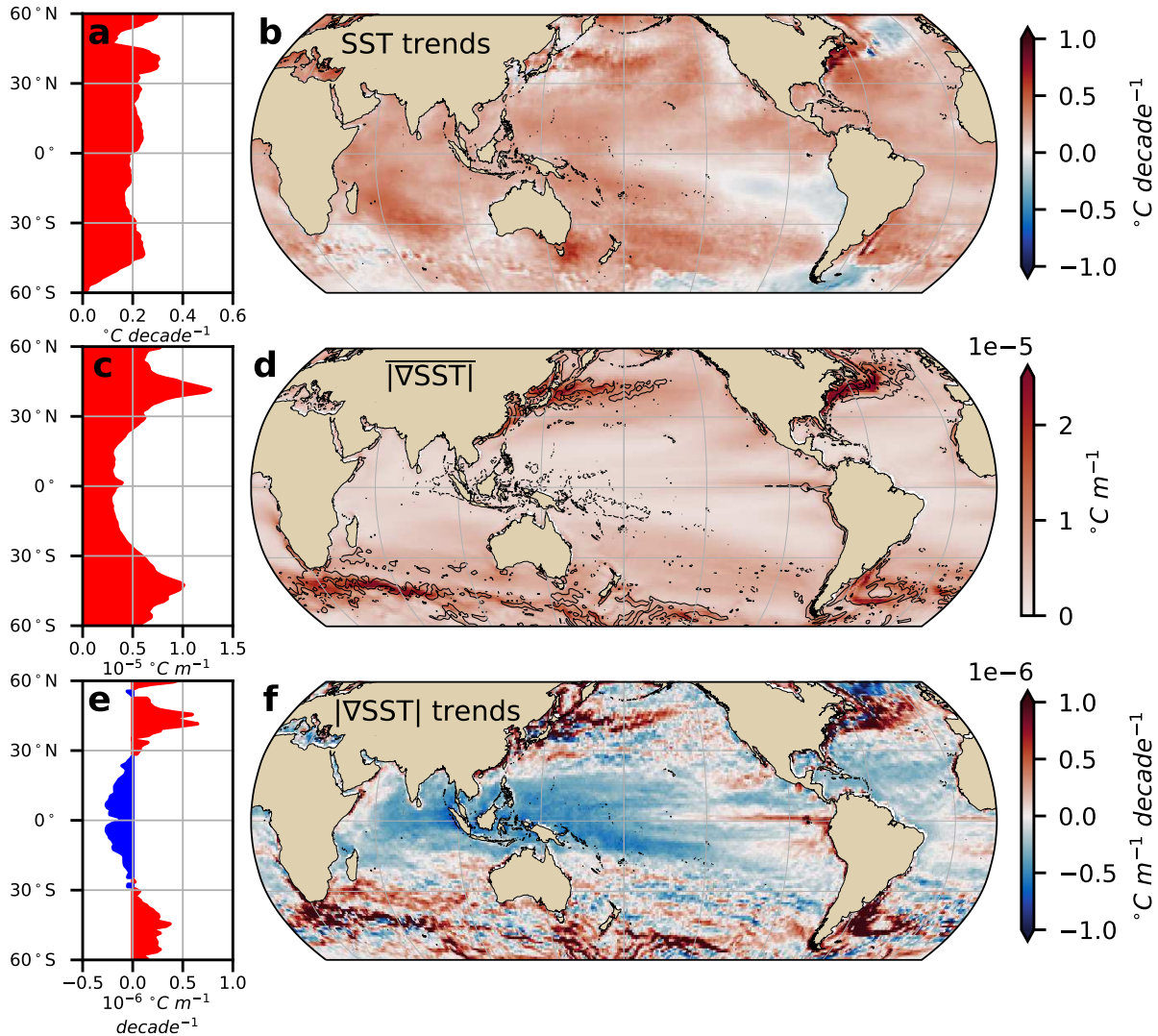
316 en/data/products/sea-surface-height-products/global/gridded-sea-level-height
317 html). All datasets are available in netCDF format at [https://doi.org/10.5281/zenodo.](https://doi.org/10.5281/zenodo.3993824)
318 3993824. Additional information and notebooks that reproduce the figures can be found at
319 https://github.com/josuemtzmo/EKE_SST_trends. J. M.-M. was supported by the
320 Consejo Nacional de Ciencia y Tecnología (CONACYT), Mexico funding. A. K. M. was sup-
321 ported by the Australian Research Council DECRA Fellowship DE170100184. Analyses were un-
322 dertaken on the National Computational Infrastructure in Canberra, Australia, which is supported
323 by the Australian Commonwealth Government.



324

325 **Figure 1 Sea Surface Height trend, mean surface Eddy Kinetic Energy and surface**
 326 **Eddy Kinetic Energy trend between 1993-2019** (a) Zonally averaged SSH trend; (b)
 327 map of SSH trend (92.1% of global area is significant above 95% confidence level; for
 328 spatial distribution refer to Fig. S1); (c) zonally averaged mean EKE; (d) map of mean
 329 EKE; (e) zonally averaged EKE trend; (f) map of EKE trend (55.4% of global area is
 330 significant above 95% confidence level). In panel (d), solid contours show positive EKE
 331 trends and dashed contours show negative EKE trends (contours of $\pm 5 J m^{-3} \text{ decade}^{-1}$).
 332

332



333

334

335

336

337

338

339

340

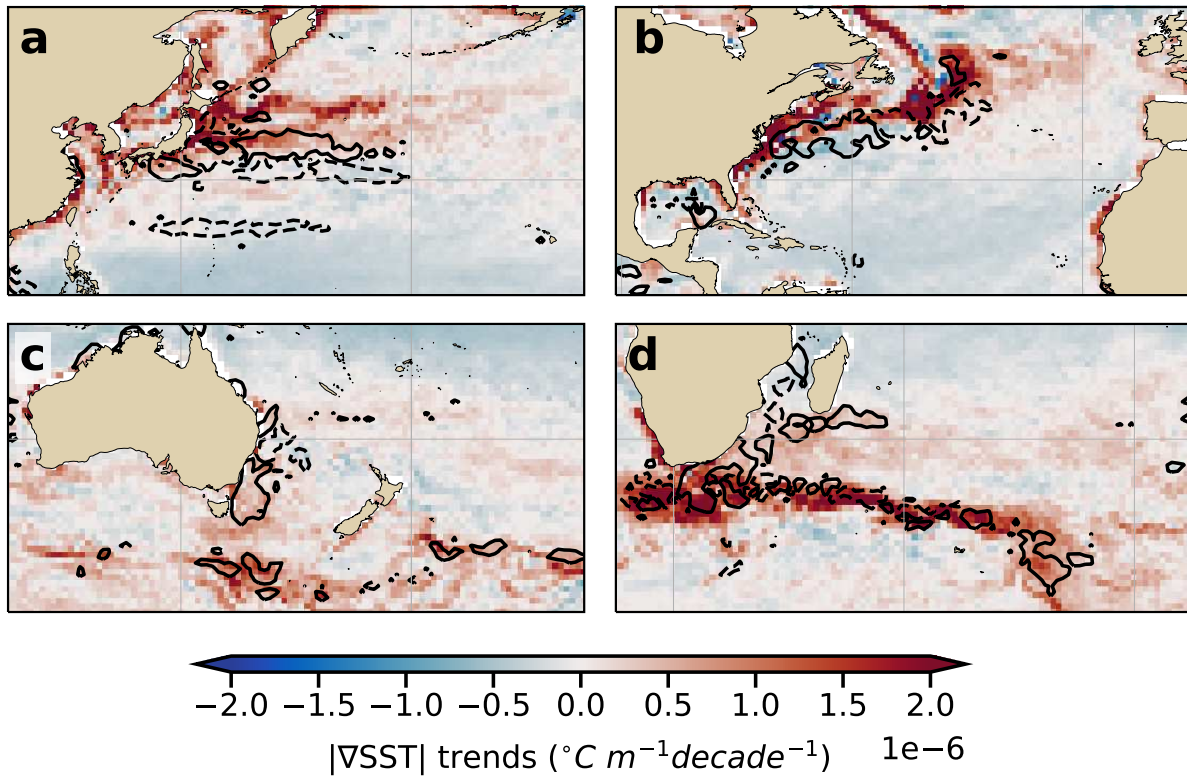
341

342

343

344

Figure 2 Sea Surface Temperature (SST) trends, mean SST gradient magnitude, and SST gradient magnitude trends between 1993-2019. (a) Zonally averaged SST trend; (b) map of SST trend (76.7% of global area is significant above 95% confidence level; for the spatial distribution refer to Fig. S1); (c) zonally averaged time-mean of SST gradient magnitude; (d) map of time-mean of SST gradients magnitude; (e) zonally averaged SST gradient trend; (f) map of SST gradient trends (81.6% of global area is significant above 95% confidence level). In panel (d), solid contours show positive SST gradient trends and dashed contours show negative SST gradient trends ($\pm 0.5 \times 10^{-6} \text{ } ^\circ\text{C m}^{-1}\text{decade}^{-1}$). Note that the spatial pattern of SST gradient maps is independent of the temporal extent of the SST gradient record used to compute SST gradient trends (Fig. S2).



345

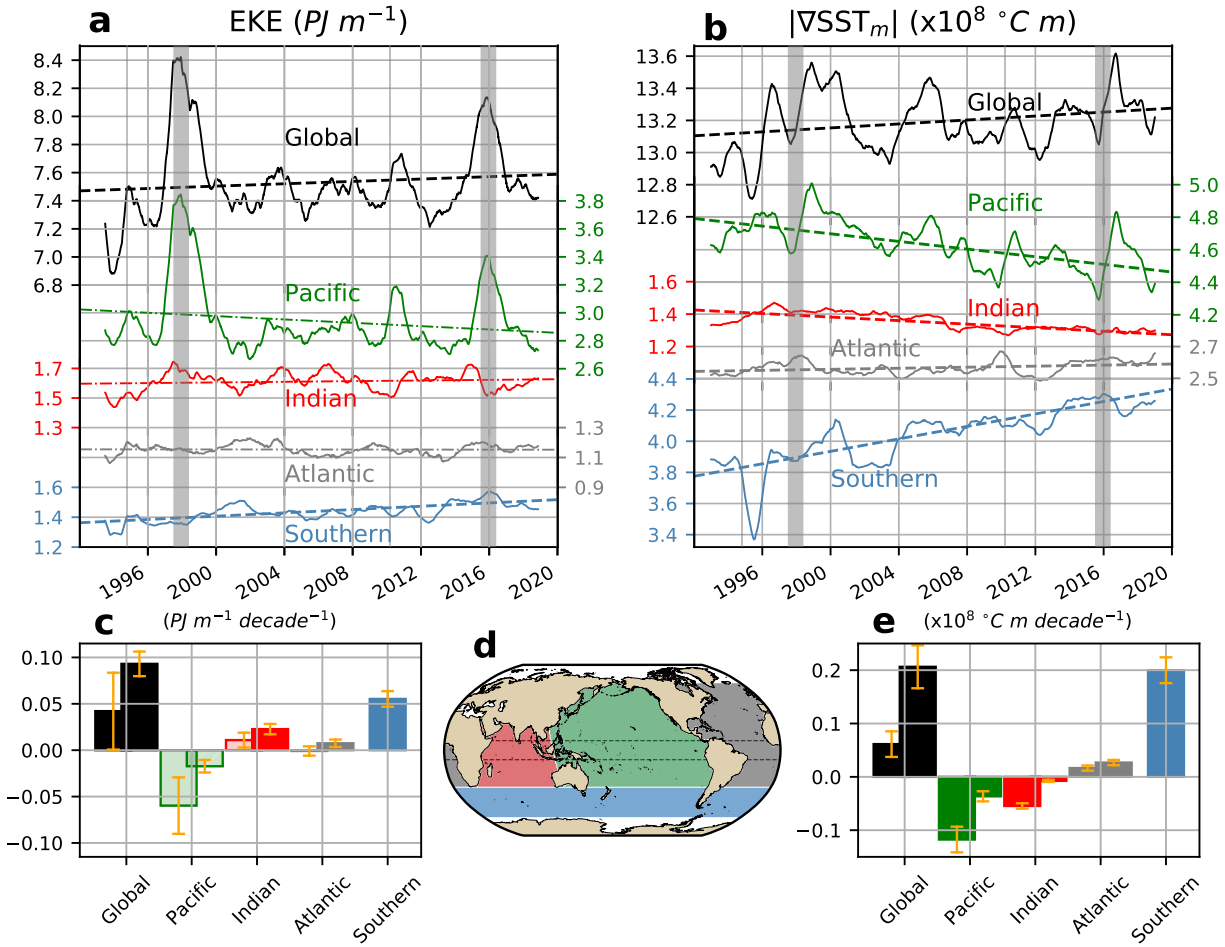
346

347

348

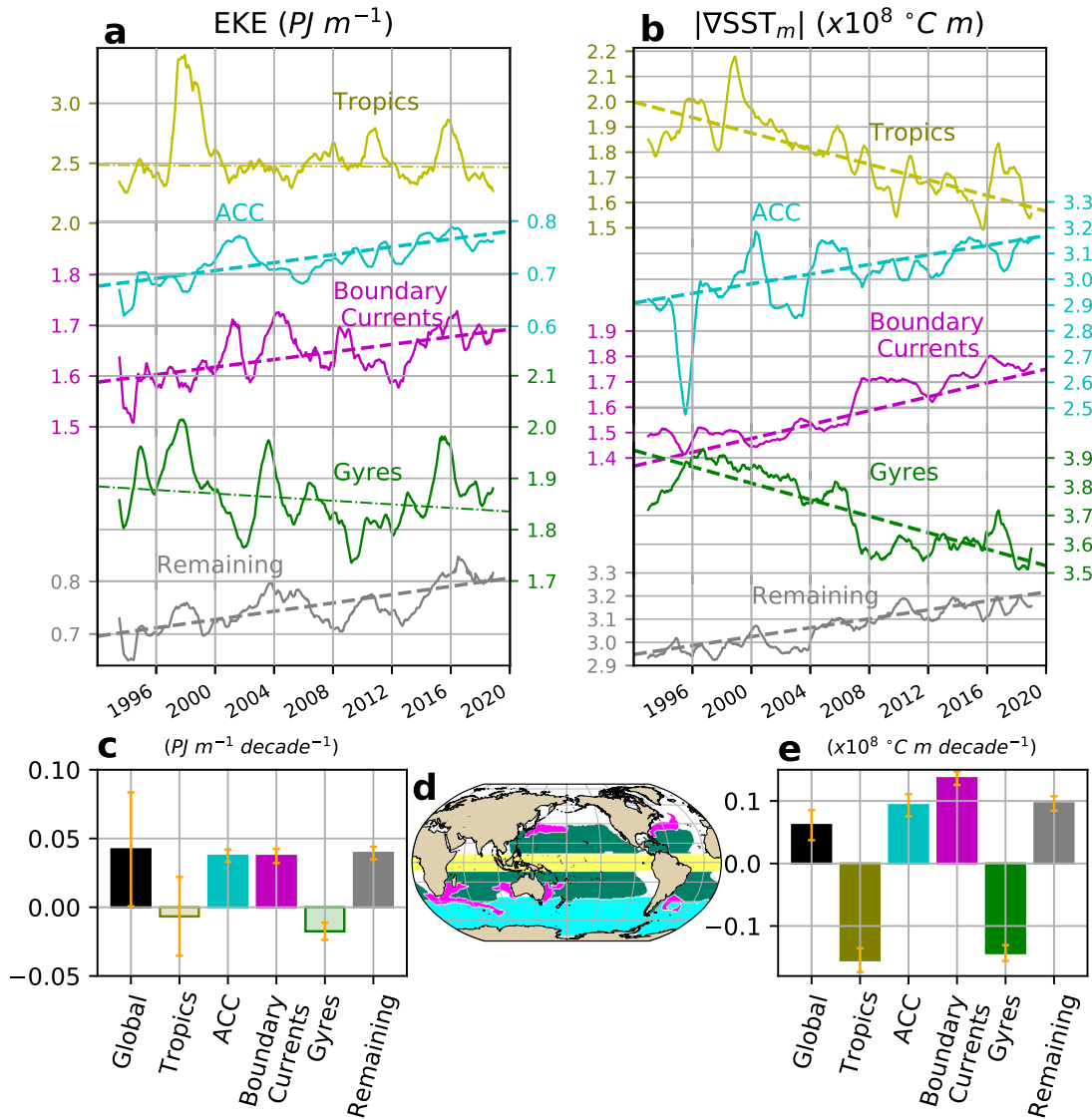
349

Figure 3 Regional maps of mesoscale SST gradient trends and EKE trends. (a) Kuroshio Current; (b) Gulf Stream; (c) East Australian Current; (d) Agulhas retroflexion. In all panels, solid contours show positive EKE trends and dashed contours show negative EKE trends (contours of $\pm 5 \text{ J m}^{-3} \text{ decade}^{-1}$).



350
 351
 352
 353
 354
 355
 356
 357
 358
 359
 360
 361
 362
 363

Figure 4 Time-series and linear trends of area integrated EKE and mesoscale SST gradients over various ocean basins. Global (solid black), Southern (blue), Indian (red), Pacific (green), and Atlantic Oceans (gray) and each region separately without the equatorial region (striped bars). (a) EKE time series. (b) mesoscale SST gradient time series. In panels (a) and (b), solid curves denote 12-month running averages for each basin, dashed lines correspond to significant time-series trend, dashed-dotted lines show insignificant time-series trend, and vertical gray bars indicate El Niño events (above the 90th percentile of MEI.v2⁴²). Note that the y axis is discontinuous in panels (a) and (b). (c) Linear EKE trends for each basin. (d) Ocean basins; equatorial region (9°S–9°N) is marked by the dashed lines. (e) Linear mesoscale SST gradient trends. In panels (c) and (e), standard errors are shown with orange bars and statistically significant trends (above 95% confidence level) denoted with solid bars while non-significant trends are translucent.



364
 365
 366
 367
 368
 369
 370
 371
 372
 373
 374
 375
 376

Figure 5 Time-series and linear trends of integrated EKE and mesoscale SST gradients over dynamical regions. Global Ocean (black), Tropics (yellow), Antarctic Circumpolar Current (cyan), Boundary Currents and their extensions (magenta), Subtropical Ocean Gyres (green) and the rest (gray). (a) EKE time series. (b) mesoscale SST gradient time series. In panels (a) and (b), solid color curves are 12-month running averages of EKE and mesoscale SST gradients for each region, dashed lines correspond to significant time-series trend, and dashed-dotted lines show insignificant time-series trend. (c) Linear EKE trends for each dynamical region. (d) Definition of ocean regions. (e) Linear mesoscale SST gradient trends. Note that in panel (a) the top curve that corresponds to the Tropics has a different scale than the rest. In panels (c) and (e), standard errors are shown with orange bars and statistically significant trends (above 95% confidence level) are solid bars while non-significant trends are translucent.

377 **Methods**

378 **Observational products**

379 The data used in this study includes Sea Surface Height, geostrophic velocities, and Sea Sur-
380 face Temperature. The Archiving, Validation and Interpretation of Satellite Oceanographic data
381 (AVISO+) gridded multimission sea surface height and geostrophic velocities have a horizontal
382 resolution of $1/4^\circ$. Currents within the equatorial region ($5^\circ S$ - $5^\circ N$) are estimated using an equa-
383 torial β -plane approximation of the geostrophic equations⁴³. National Oceanic and Atmospheric
384 Administration - Optimum Interpolation Sea Surface Temperature (NOAA-OISST) has a hori-
385 zontal resolution of $1/4^\circ$ ²³. This dataset is constructed by combining observations from different
386 products (e.g. satellites, ships, buoys, and ARGO floats).

387 These datasets have a quasi-global coverage ($65^\circ S$ - $65^\circ N$) and span 26 years, from January
388 1993 to December 2019. Anomalies were computed with respect to the record's climatology.
389 We have verified that using a different period for defining the climatology does not change the
390 observed trends in the anomaly fields. Moreover, through wavelet analysis (edge detection) of the
391 time-series, we have verified that the observed trends are not a product of steps in the number of
392 satellite missions and oceanographic observations.

393 **Kinetic Energy decomposition**

394 Kinetic energy density is decomposed into the energy density contained by the steady flow
395 (time-mean) and that contained by the transient flow (time-varying). In other words, the surface
396 geostrophic velocity components are split using a Reynolds decomposition into their time-mean

397 (\bar{u}, \bar{v}) and time-varying components ($u' = u - \bar{u}$, $v' = v - \bar{v}$), with bars denoting time-averages
 398 over the whole record. The KE is, therefore, decomposed as:

$$399 \quad \underbrace{\frac{1}{2}\rho_0 (u^2 + v^2)}_{\text{KE}} = \underbrace{\frac{1}{2}\rho_0 (u'^2 + v'^2)}_{\text{EKE}} + \underbrace{\frac{1}{2}\rho_0 (\bar{u}^2 + \bar{v}^2)}_{\text{MKE}} + \underbrace{\rho_0(\bar{u}u' + \bar{v}v')}_{\text{Cross terms}}, \quad (1)$$

400 where we approximate the density of the seawater by the constant $\rho_0 = 1025 \text{ kg m}^{-3}$. The
 401 energy contained in the time-varying component of the flow is known as the eddy kinetic energy
 402 (EKE), while the mean kinetic energy (MKE) is the energy of the time-mean flow.

403 Maps of EKE in this study correspond to the the time-mean EKE, defined as

$$404 \quad \overline{\text{EKE}}(x, y) = \overline{\frac{1}{2}\rho_0(u'^2 + v'^2)}. \quad (2)$$

405 Time-series correspond to the surface integrated EKE (globally or over specific regions),

$$406 \quad \langle \text{EKE} \rangle(t) = \iint_A \frac{1}{2}\rho_0(u'^2 + v'^2) dx dy, \quad (3)$$

407 where A refers to the area of each geographical or dynamical region, u' and v' are anomalies of
 408 the surface geostrophic velocities provided by AVISO+, and angle brackets $\langle \rangle$ denote the area
 409 integral.

410 **Sea surface temperature gradients**

411 Sea surface temperature (SST) gradients are decomposed into mesoscale (SST gradients with
 412 scales smaller than 3°) and large-scale (SST gradients with scales larger than 3°). To decompose
 413 the SST gradients, we first compute large-scale SST by using an average spatial convolution of

414 $3^\circ \times 3^\circ$, and a 12-months running average i.e.,

$$415 \quad \text{SST}_{ls}(x, y, t) = \frac{\iint \widetilde{\text{SST}}(x - x', y - y', t) K(x', y') dx' dy'}{\iint K(x', y') dx' dy'}, \quad (4)$$

416 where the SST field is convolved with a constant $3^\circ \times 3^\circ$ kernel K and the tilde $\widetilde{}$ denotes a
417 12-month running average. The mesoscale SST is then defined as

$$418 \quad \text{SST}_m = \text{SST} - \text{SST}_{ls}. \quad (5)$$

419 Small-scale EKE was computed analogously to the mesoscale SST but for the velocity components
420 ($u_m = u - u_{ls}$, $v_m = v - v_{ls}$).

421 The gradients of the large-scale and mesoscale SST are computed afterwards. The SST
422 gradient magnitude is:

$$423 \quad |\nabla \text{SST}| = \sqrt{\left(\frac{\partial \text{SST}}{\partial x}\right)^2 + \left(\frac{\partial \text{SST}}{\partial y}\right)^2}, \quad (6)$$

424 with analogous expressions for SST_m and SST_{ls} .

425 Computations of SST gradient time-series and time mean SST gradient trend maps are anal-
426 ogous to those of EKE, namely:

$$427 \quad \langle |\nabla \text{SST}| \rangle(t) = \iint_A |\nabla \text{SST}| dx dy, \quad (7)$$

428 **Trends, significance & uncertainties**

429 Linear trends are calculated using a linear least-squares regression model for spatial inte-
430 grated time-series and geographic data. The fields are first coarsened to a $1^\circ \times 1^\circ$ grid, and then
431 the linear trends are computed for each grid point.

432 A modified Mann-Kendall test is used to assess statistical significance of trends, while prop-
433 erly taking into account the autocorrelation in the time-series²⁴. The effective sample size for all
434 the reported trends is always smaller than the actual sample size, due to autocorrelation of the
435 time series. The significance of our observed trends for EKE and SST gradients is assessed via
436 a t-student distribution test. If the probability of the trend is smaller than the confidence level
437 ($\alpha = 0.05$) then the null hypothesis is rejected and the estimated slope is considered significant
438 at the 95% confidence level. The Pearson coefficient was also used to assess the significance of
439 the trends. If the Pearson coefficient is smaller than 0.05 for a significance level of 95%, then the
440 existing trend is considered to be statistically significant. Finally, the reported uncertainties corre-
441 spond to the standard error using the effective sample size from the Mann-Kendall test; that is, the
442 standard deviation of the time-series divided by the square root of the effective sample size.

443 **Geographical and dynamical regions**

444 Geographical regions consist of the following ocean basins: the Southern Ocean, the In-
445 dian Ocean, the Pacific Ocean and the Atlantic Ocean. These ocean basins were defined to cap-
446 ture ocean processes at all scales. The ocean basin mask can be obtained from the repository
447 https://github.com/josuemtzmo/EKE_SST_trends that contains all the data used for
448 this study (refer to acknowledgments; filename `ocean_basin_mask.nc`).

449 Dynamical regions were defined from the climatological mean SSH and the mean KE. We
450 define a mask for each dynamical region and overlay the masks on a global mask in the follow-
451 ing order. First, the Antarctic Circumpolar Current (ACC) is defined as all regions south of 35°S.

452 Second, the subtropical ocean gyre definitions depend on the particular ocean basin they are lo-
453 cated within: the Pacific Ocean gyres correspond to mean SSH above the 0.65 *m* contour; the
454 Atlantic Ocean gyres correspond to mean SSH above the 0.36 *m* contour; and the Indian Ocean
455 gyres correspond to mean SSH above the 0.60 *m* contour. All these values were tuned to cap-
456 ture approximately the same extension as the theoretical estimation of ocean gyres according
457 to the Sverdrup balance. Third, the boundary currents and their extensions are defined as re-
458 gions with mean KE above the ~ 99 -th percentile (2.8σ). Lastly, the equatorial region is de-
459 fined as the region between 9°S and 9°N. The dynamical regional mask can be obtained from
460 the repository containing all the data used for this study (refer to acknowledgments; filename
461 `ocean_processes_mask.nc`).

Figures

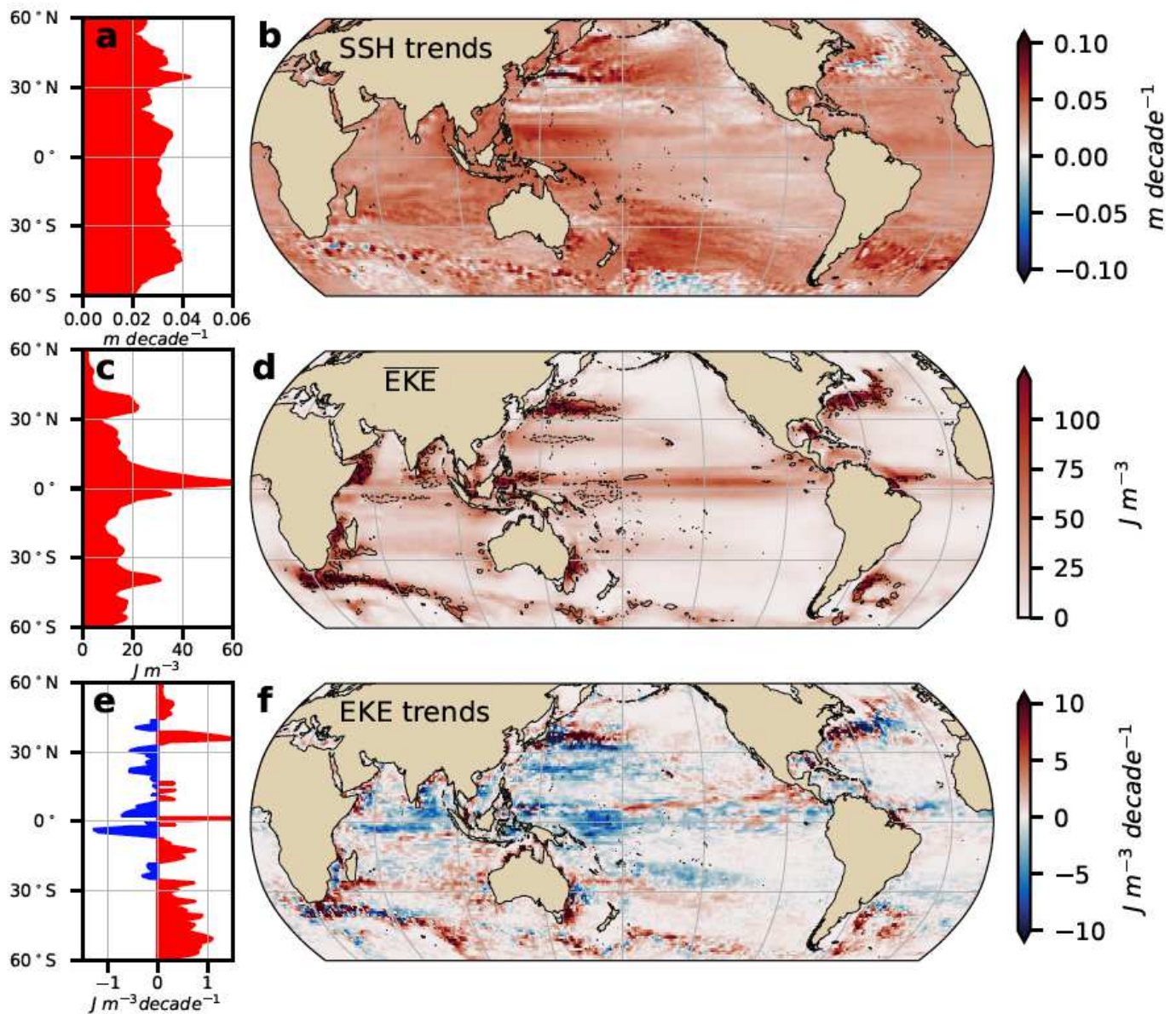


Figure 1

Sea Surface Height trend, mean surface Eddy Kinetic Energy and surface Eddy Kinetic Energy trend between 1993-2019 (a) Zonally averaged SSH trend; (b) map of SSH trend (92.1% of global area is significant above 95% confidence level; for spatial distribution refer to Fig. S1); (c) zonally averaged mean EKE; (d) map of mean EKE; (e) zonally averaged EKE trend; (f) map of EKE trend (55.4% of global area is significant above 95% confidence level). In panel (d), solid contours show positive EKE trends and dashed contours show negative EKE trends (contours of $\pm 5 \text{ J m}^{-3} \text{ decade}^{-1}$). Note: The designations employed and the presentation of the material on this map do not imply the expression of any opinion whatsoever on the part of Research Square concerning the legal status of any country, territory, city or area or of its

authorities, or concerning the delimitation of its frontiers or boundaries. This map has been provided by the authors.

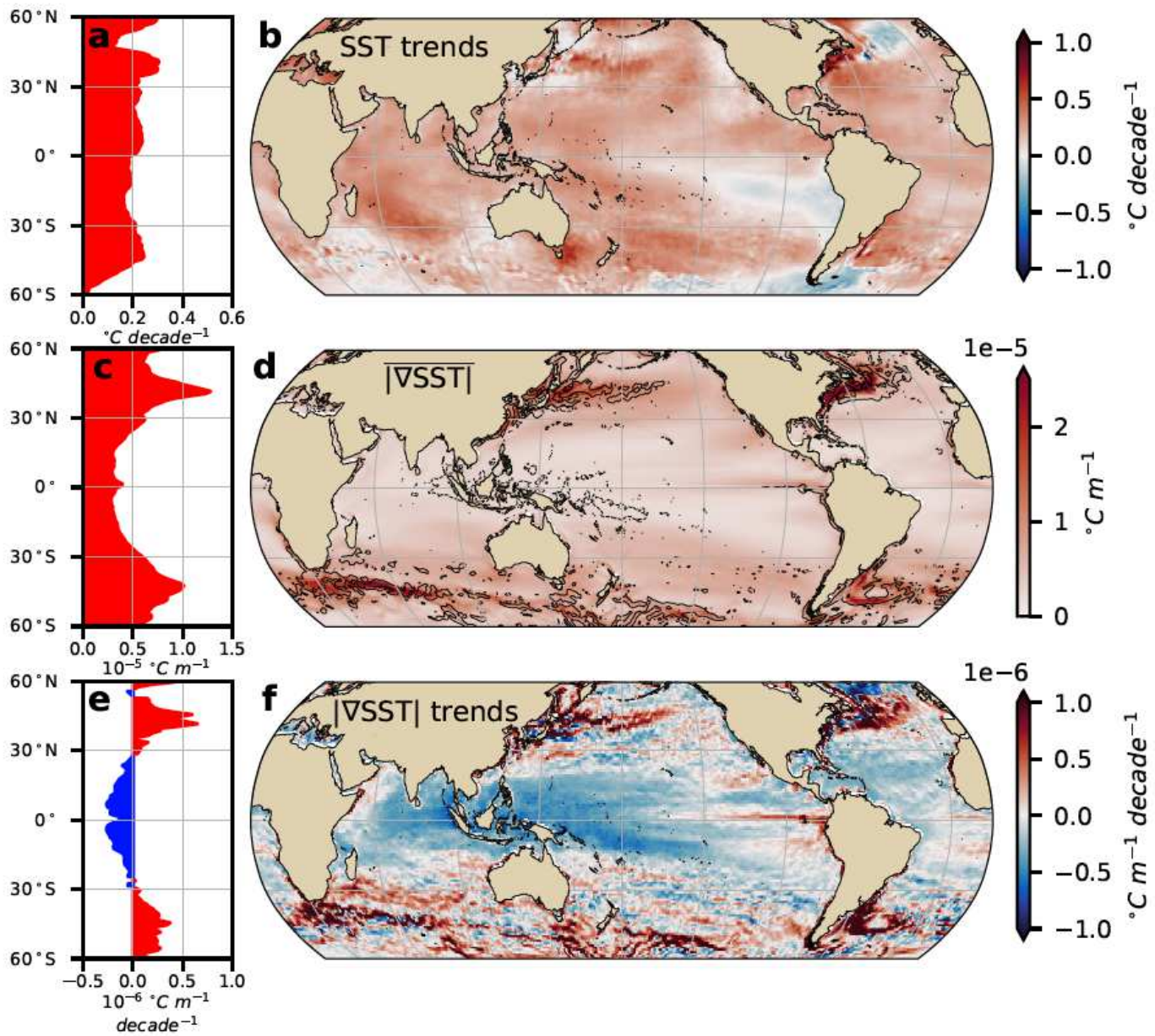


Figure 2

Sea Surface Temperature (SST) trends, mean SST gradient magnitude, and SST gradient magnitude trends between 1993-2019. (a) Zonally averaged SST trend; (b) map of SST trend (76.7% of global area is significant above 95% confidence level; for the spatial distribution refer to Fig. S1); (c) zonally averaged time-mean of SST gradient magnitude; (d) map of time-mean of SST gradients magnitude; (e) zonally averaged SST gradient trend; (f) map of SST gradient trends (81.6% of global area is significant above 95% confidence level). In panel (d), solid contours show positive SST gradient trends and dashed contours show negative SST gradient trends ($\pm 0.5 \times 10^{-6} \text{ } ^\circ\text{C m}^{-1}\text{decade}^{-1}$). Note that the spatial pattern of SST gradient maps is independent of the temporal extent of the SST gradient record used to compute

SST gradient trends (Fig. S2). Note: The designations employed and the presentation of the material on this map do not imply the expression of any opinion whatsoever on the part of Research Square concerning the legal status of any country, territory, city or area or of its authorities, or concerning the delimitation of its frontiers or boundaries. This map has been provided by the authors.

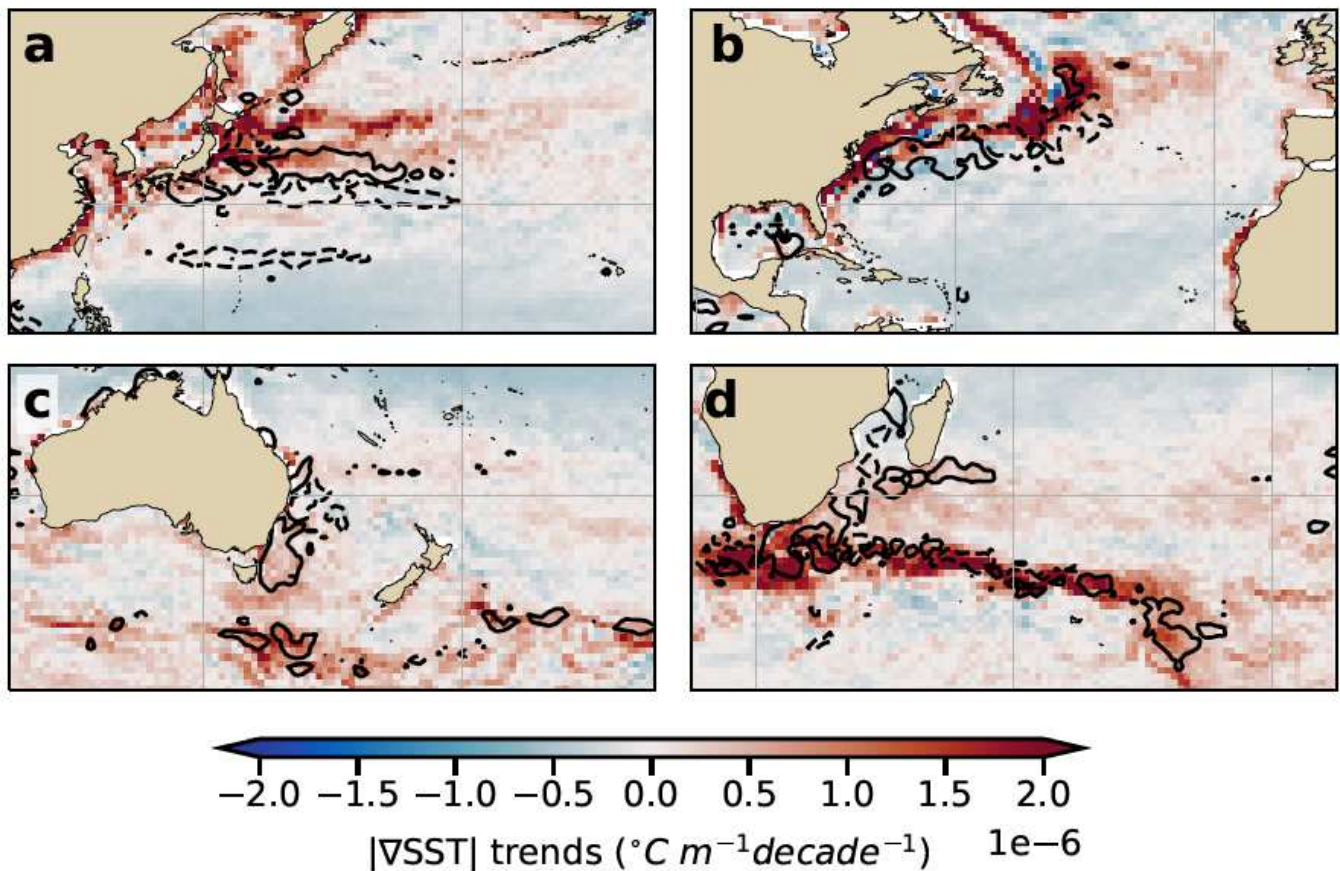


Figure 3

Regional maps of mesoscale SST gradient trends and EKE trends. (a) Kuroshio Current; (b) Gulf Stream; (c) East Australian Current; (d) Agulhas retroflexion. In all panels, solid contours show positive EKE trends and dashed contours show negative EKE trends (contours of $\pm 5 \text{ J m}^{-3} \text{ decade}^{-1}$). Note: The designations employed and the presentation of the material on this map do not imply the expression of any opinion whatsoever on the part of Research Square concerning the legal status of any country, territory, city or area or of its authorities, or concerning the delimitation of its frontiers or boundaries. This map has been provided by the authors.

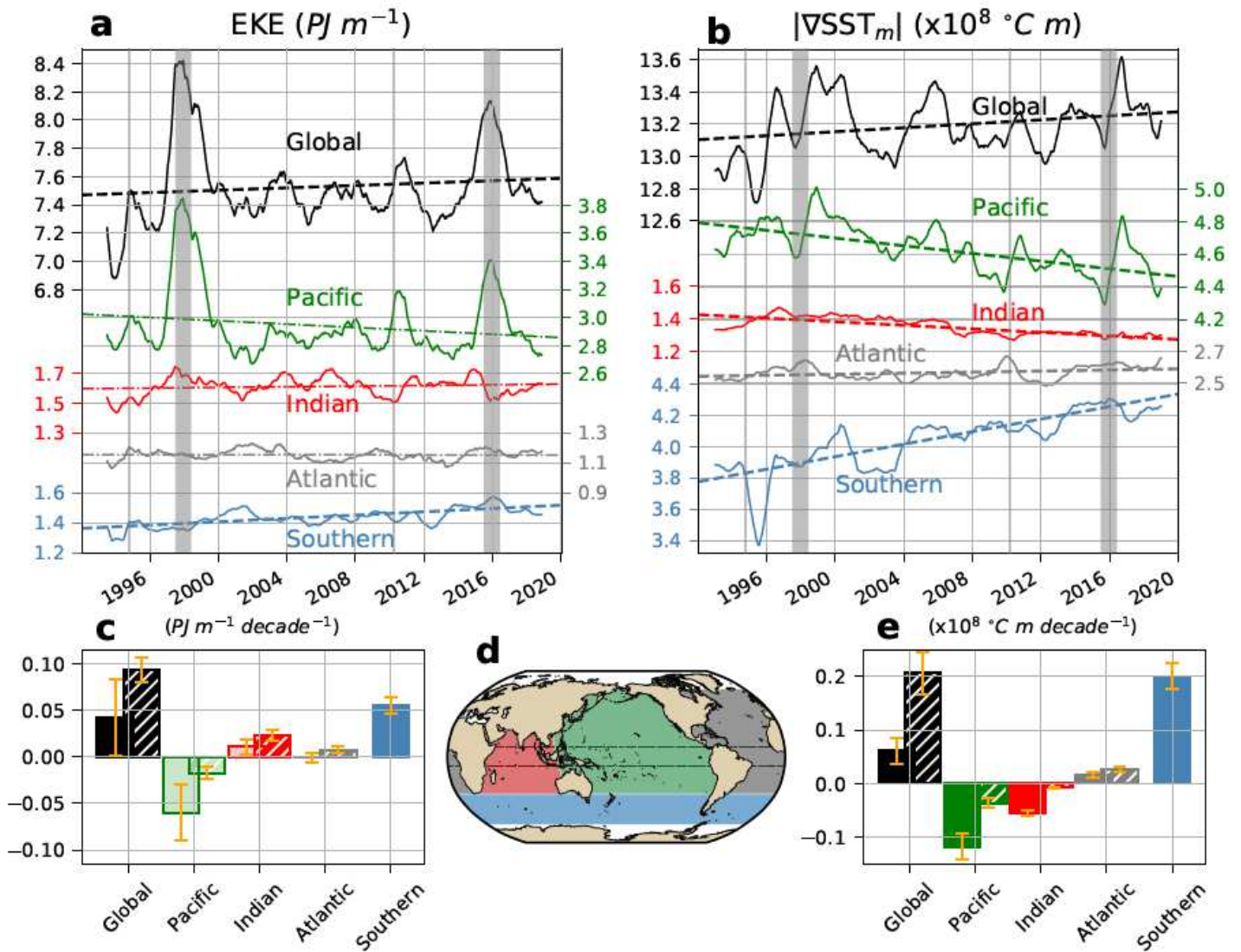


Figure 4

Time-series and linear trends of area integrated EKE and mesoscale SST gradients over various ocean basins. Global (solid black), Southern (blue), Indian (red), Pacific (green), and Atlantic Oceans (gray) and each region separately without the equatorial region (striped bars). (a) EKE time series. (b) mesoscale SST gradient time series. In panels (a) and (b), solid curves denote 12-month running averages for each basin, dashed lines correspond to significant time-series trend, dashed-dotted lines show insignificant time-series trend, and vertical gray bars indicate El Niño events (above the 90th percentile of MEI.v242). Note that the y axis is discontinuous in panels (a) and (b). (c) Linear EKE trends for each basin. (d) Ocean basins; equatorial region ($9^\circ S-9^\circ N$) is marked by the dashed lines. (e) Linear mesoscale SST gradient trends. In panels (c) and (e), standard errors are shown with orange bars and statistically significant trends (above 95% confidence level) denoted with solid bars while non-significant trends are translucent. Note: The designations employed and the presentation of the material on this map do not imply the expression of any opinion whatsoever on the part of Research Square concerning the legal status of any

country, territory, city or area or of its authorities, or concerning the delimitation of its frontiers or boundaries. This map has been provided by the authors.

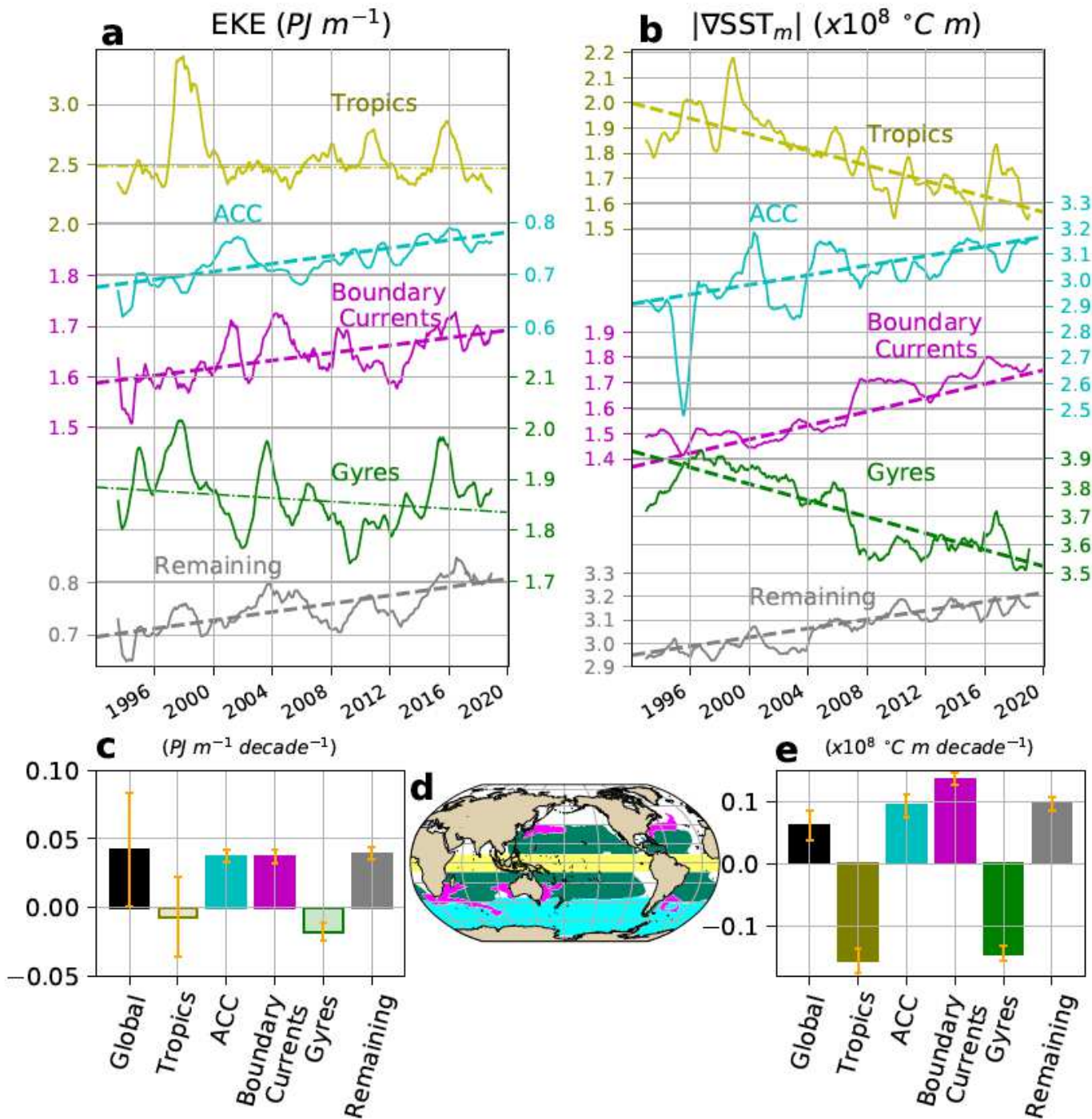


Figure 5

Time-series and linear trends of integrated EKE and mesoscale SST gradients over dynamical regions. Global Ocean (black), Tropics (yellow), Antarctic Circumpolar Current (cyan), Boundary Currents and their extensions (magenta), Subtropical Ocean Gyres (green) and the rest (gray). (a) EKE time series. (b) mesoscale SST gradient time series. In panels (a) and (b), solid color curves are 12-month running averages of EKE and mesoscale SST gradients for each region, dashed lines correspond to significant

time-series trend, and dashed-dotted lines show insignificant time-series trend. (c) Linear EKE trends for each dynamical region. (d) Definition of ocean regions. (e) Linear mesoscale SST gradient trends. Note that in panel (a) the top curve that corresponds to the Tropics has a different scale than the rest. In panels (c) and (e), standard errors are shown with orange bars and statistically significant trends (above 95% confidence level) are solid bars while non-significant trends are translucent. Note: The designations employed and the presentation of the material on this map do not imply the expression of any opinion whatsoever on the part of Research Square concerning the legal status of any country, territory, city or area or of its authorities, or concerning the delimitation of its frontiers or boundaries. This map has been provided by the authors.

Supplementary Files

This is a list of supplementary files associated with this preprint. Click to download.

- [OceancurrentchangesJMMsupplementary.pdf](#)